J Mater Sci (2022) 57:2180–2193

Metals & corrosion

Effect of plastic deformation on the precipitation sequence of 2024 aluminum alloy

J. C. Guía-Tello[1], C. G. Garay-Reyes[1,*], G. Rodríguez-Cabriales[1], H. M. Medrano-Prieto[2], M. A. Ruiz-Esparza-Rodríguez[1], L. J. García Hernández[1], J. M. Mendoza-Duarte[1], K. A. García-Aguirre[1], I. Estrada-Guel[1], S. González[3], and R. Martínez-Sánchez[1,*]

[1] *Centro de Investigación en Materiales Avanzados (CIMAV), Laboratorio Nacional de Nanotecnología, Miguel de Cervantes No. 120, C.P. 31109 Chihuahua, Chih, México*

[2] *Universidad Tecnológica de Chihuahua Sur. Km. 3 Carretera Chihuahua-Aldama S/N, C.P. 31313 Chihuahua, Chih, México*

[3] *Faculty of Engineering and Environment, Northumbria University, Newcastle upon Tyne NE1 8ST, UK*

Received: 30 August 2021
Accepted: 1 November 2021
Published online: 3 January 2022

ABSTRACT

The present study aims to evaluate plastic deformation's effect by cold-rolling on the precipitation sequence of 2024 aluminum alloy. X-ray diffraction, scanning/transmission electron microscopy, and Vickers microhardness tests have been used to characterize the microstructure and mechanical behavior of the alloys. It was observed that plastic deformation induces changes in the precipitation sequence, which affects the mechanical properties and delays the overaging stage. In the deformed alloy, two hardening peaks were observed. These peaks occurred at 30 min (248 HV ± 5) and 600 min (230 HV ± 2) and were attributed to the θ′ and S′ phases, respectively. However, in the non-deformed alloy, only a single hardening peak was observed. This peak arose after 300 min aging (208 HV ± 4) and was attributed to the S′ phase formation. Thus, the precipitation sequence in the deformed alloy was the following: αSSS–CuMg clusters → GPB-II zones/θ′′/θ′/ → S′ → S, and for the non-deformed alloy was αSSS–CuMg clusters → GPB-II zones/S′/ → S.

Handling Editor: Catalin Croitoru.

Address correspondence to E-mail: carlos.garay@cimav.edu.mx; roberto.martinez@cimav.edu.mx

https://doi.org/10.1007/s10853-021-06689-1

GRAPHICAL ABSTRACT

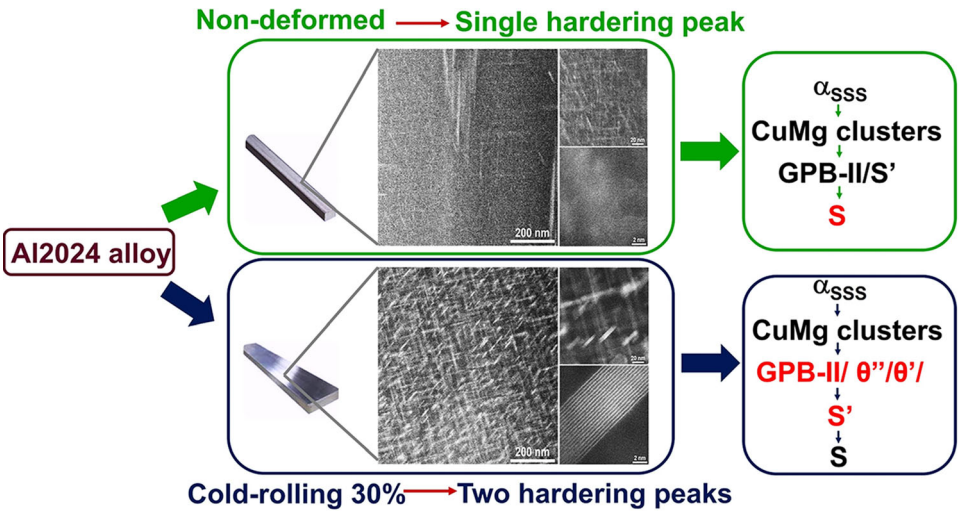

Introduction

The 2024 (Al-Cu-Mg) aluminum alloy is commonly used in commercial aircraft structures such as the fuselage and lower wing surface due to its excellent damage tolerance, high resistance to fatigue crack propagation, and fracture toughness [1]. Besides, precipitation hardening is widely used to strengthen this alloy because the formed precipitates are crystallographically coherent with the aluminum matrix, and their fine dispersion enhances the mechanical properties of the alloys [2]. In this regard, the primary precipitates in Al-Cu-Mg alloy have been generally identified as S′ phase (Al_2CuMg), θ′ phase (Al_2Cu), and Guinier–Preston–Bagaryatsky zones (GPB) [3, 4]. On the other hand, it is well known that the processing conditions can influence the precipitation of those phases, resulting in different microstructures and properties. However, various studies agree that the main effect of the plastic deformation in the Al-Cu-Mg alloy system is the variation in size, distribution, and sequence of precipitates, which affect the mechanical performance by enhancing the strength of the alloy system [5, 6]. It has been reported that in the Al-Cu-Mg alloy system, 5% of pre-straining increases the number density of the S precipitates, and the overaging stage was shortened depending on the increment of pre-strain [7]. Additionally, the number density of GPB zones decreases as the pre-strain increases. i.e., when the pre-strain is up to 5%, S precipitates are predominant to the peak-aged. This fine uniform distribution of S precipitates leads to a higher hardness than when only GPB zones are present. However, pre-straining up to 15% before aging is critical to the density of dislocations generated and decreases the average diameter of the precipitates [8].

On the other hand, it has been reported that when the Al-Cu-Mg alloy system is subjected to a deformation of 8% followed by aging, the microhardness curve exhibits a single peak-aged at 180 min (170 HV) [9]. This behavior was attributed to the progressive formation of semicoherent S′ precipitates. It has also been shown that thermo-mechanical treatment provides a uniform deformation and produces a fine distribution of θ precipitates on the dislocations, which improves the fatigue behavior of the aluminum alloy due to the fine size of the θ precipitates that inhibit dynamic recovery [10]. In addition, when the Al-Cu-Mg alloy system is subjected to different levels of deformation, interesting microhardness results occur due to the formation of fine S′ precipitates and further formation of Ω phase from the S′ precipitates [11].

Another research work carried out in an aluminum alloy with low magnesium, pre-strained at 75% and aged at 190 °C, showed a microhardness curve with two well-defined peaks after the aging. At 180 min aging, the first maximum hardness occurred due to the θ'' phase (145 HV). The second maximum hardness occurred after 720 min and was associated with the presence of θ'' and θ' (148 HV) phases, while during overaging, the θ' and θ phases replace the θ'' phase. In addition, precipitation of the Ω phase was observed, but its numerical density was relatively low [12]. In this regard, a study performed in the Al-Cu-Mg alloy system aged at 180 °C showed a microhardness increase, while that the time to reach the peak-aged condition was reduced with increasing pre-strain. The maximum microhardness value (187 HV at 190 min aging) was attained when the alloy system was cold-rolled to 40% and was attributed to the precipitation of the S'(AlCuMg) phase. In addition, studies by TEM showed that cold-rolling increases the number density of the S' phase, but the size of the precipitates decreases with the increase of pre-strain [13]. More recently, the effect of cold-rolling on double stage aging (60°C-1 h-180°C-1 h) in AA2024 aluminum alloy was studied [14]. The results showed that cold-rolling to 50% provided a higher strength level (190 HV) than cold-rolling to 25% (167 HV). In both conditions, the lower aging temperature leads to the formation of clusters and GPB zones that are spread out due to dislocations. Subsequent aging at 180°C led to the growth of these clusters and GPB zones and precipitation of S and θ phases.

It is worth to be noted that in the previous lab-scale studies, where the thermal shock is dismissed, the quenching at room temperature was widely used. However, industrial processes generally use quenching temperatures close to 60° C to prevent dimensional defects generated by thermal shock. Despite the extensive research on the precipitation in Al-Cu-Mg alloy, previous studies have ignored the quenching condition higher than room temperature. In this regard, the thermo-mechanical process with an initial quenching at 60°C followed by plastic deformation by cold-rolling and artificial aging has not been reported elsewhere. Moreover, the processing-microstructure-microhardness correlation in the aged 2024 aluminum alloy has been established in this work. The results are analyzed in detail, and a novel precipitation sequence is proposed. This new knowledge could be helpful in the industrial production of 2024 aluminum alloy to enhance its mechanical properties. In this study, plastic deformation processing accelerates the precipitation of phases, which reduces the aging time to achieve high microhardness values compared to that previously reported in the literature. Therefore, the proposed thermo-mechanical process could have implications at the industrial levels, such as an energy-saving method, by decreasing the aging time and thus increasing the production velocity of the 2024 aluminum alloy while achieving better mechanical properties.

Experimental

A commercial 2024 aluminum alloy was used as raw material, and its chemical composition was determined using a spectrometer Spectromaxx with iCAL 2.0 (see Table 1). The alloy was melted in a Lindberg BlueTM electric furnace at 740° C. The melted alloy was degassed with argon gas (20 Psi) for 15 min and 0.33 wt. % of Al-5Ti-1B was added as a grain refiner. The alloy was poured into cylindrical steel molds and hot-extruded to 465°C to produce rectangular bars with an extrusion ratio of 16. The solution heat treatment (SHT) was carried out in a Lindberg BlueTM electric furnace at 495° C for 420 min, followed by quenching in water at 60 °C. After SHT, the 2024 aluminum alloy was prepared in two different states: one set of samples was deformed by cold rolling (CR) up to 30% thickness reduction. Another set of non-deformed samples was selected as the reference for comparison purposes. Afterward, aging heat treatment (AHT) was performed in a Felisa TM furnace for all deformed and non-deformed samples. The conditions of AHT were 195 °C for 30, 60, 300, 600, 3000, and 6000 min, followed by quenching in water at room temperature. The studied conditions were: as-cast, extruded, solubilized, deformed-aged, and non-deformed-aged. Vickers microhardness (HV) tests were performed in a LECO LM300AT hardness tester using a 50 g load and 10 s dwell time at every processing step. An average of 10 indentations for each sample was carried out. Additionally, the structure evolution was followed by X-ray diffraction (XRD), and the microstructure was characterized using a scanning electron microscope equipped with an energy-dispersive X-ray

Table 1 Chemical composition of the 2024 aluminum alloy (wt. %)

Al	Cu	Mg	Si	Fe	Mn	Others	Cu/Mg
Balanced	4.789	1.432	0.390	0.216	0.740	0.133	3.344

spectroscope (SEM–EDS) and a transmission electron microscope (TEM).

Analyses by XRD were performed in a Panalytical X'Pert PRO diffractometer operated at 40 kV and 30 mA using Cu Kα radiation (λ = 0.15406 nm). SEM–EDS characterization was carried out in a Hitachi SEM model SU3500 operated at 10 kV and equipped with an Oxford Microanalysis System model AZtec X-MaxN. TEM samples were prepared by Focused Ion Beam (FIB) and posteriorly cleaned in a Fischione Instruments Model 1020 Plasma Cleaner. TEM and STEM mode analyses were made in a transmission electron microscope JEM 2200 FS + CS operated at 200 kV. During these analyses, samples were oriented along the zone axis [001]. The simulation of the phase was carried out using Carine Software, and length measurement was performed employing Software ImageJ.

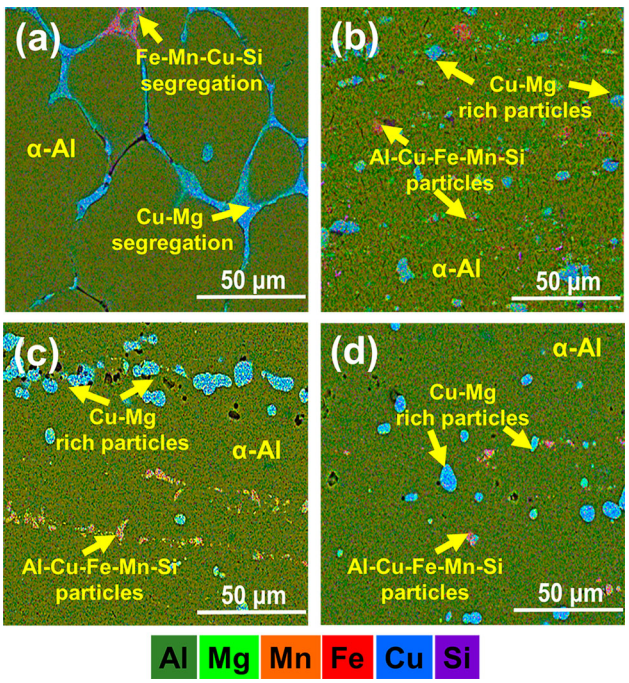

Figure 1 SEM–EDS micrographs of the 2024 aluminum alloy: **a** As-cast; **b** Extruded; **c** Solubilized; **d** cold-rolling 30%.

Results

Effect of the processing on the microstructure previous to the aged treatment

Figure 1 shows the mapping by energy-dispersive X-ray spectroscopy (SEM–EDS) of the 2024 aluminum alloy under different processing conditions before the aged treatment. In the as-cast state (Fig. 1a), the microstructure is mainly constituted by α-Al grains surrounded by an interdendritic phase, consisting of Cu and Mg and intermetallic phases rich in Cu-Fe–Mn-Si. However, the hot-extrusion process generates fragmentation of the interdendritic and leads to the formation of irregular particles rich in the same elements and oriented along the extrusion direction (Fig. 1b).

The SHT that was carried out after the hot-extrusion partially dissolves the solute elements into the α-Al matrix. Thus, resulting in the formation of some solute-rich semi-spherical and irregular particles (Fig. 1c) [15, 16]. This phenomenon occurs because the concentration of alloying elements exceeds the solubility limit of the aluminum matrix, which originates the segregation of semi-spherical particles [15]. Instead, when cold-rolling to 30% was performed, the

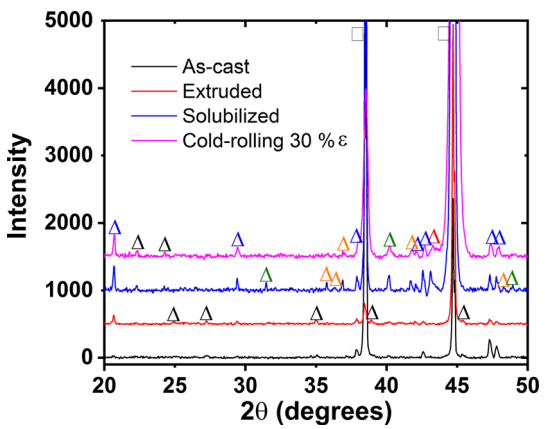

Figure 2 XRD patterns for the Al2024 alloy in as-cast, extruded, solubilized, and cold- rolling 30%. Symbols represent the following: white square α-Al, blue triangle Al_2Cu, black triangle Al_2CuMg, orange triangle Al_2Mg, red triangle $AlCu_4$, red triangle AlCu.

plastic deformation applied to the alloy induces breaking of the insoluble particles previously mentioned and heterogeneous distribution of these particles in the metallic matrix (Fig. 1d). This breaking is carried out because insoluble particles are more sensitive to the strain arising from the aluminum matrix due to deformation mismatch between the particles and metallic matrix, which causes a stresses concentration around the particles [17].

Figure 2 shows X-Ray diffraction analyses of 2024 aluminum alloy under the as-cast, extruded, solubilized, and cold-rolling conditions. The identified phases correspond to α-Al, AlCu, Al_2Cu, $AlCu_4$, Al_2CuMg, and Al_2Mg. For the as-cast and extrusion conditions, the X-ray peaks can be associated with Al_2Cu and Al_2CuMg phases. Additional phases to those detected in the as-cast and extruded conditions are observed after solubilization and cold-rolling to 30%. These phases are AlCu, $AlCu_4$, and Al_2Mg.

It is essential to mention that the change in the intensity of some of the peaks associated with the different phases indicates a texture phenomenon originating from the extrusion process. Significantly changes in the intensity of the X-ray peaks were not observed in the diffractogram after cold-rolling 30%. However, it is worth noting that the cold-rolling has an important effect during the subsequent AHT, which modifies the precipitation mechanism and improves the mechanical properties of the alloy.

Effect of the plastic deformation on the precipitation sequence

Figure 3 shows high-angle annular-dark-field images obtained by scanning-transmission electron microscopy (HAADF-STEM) corresponding to aged 2024 aluminum alloys at 195 °C for different times. For non-deformed alloy, after 30 min of aging (Fig. 3a), the α-Al matrix consists of several regions of bright contrast. The observed regions are attributed to copper clusters of 1–2.5 nm distributed homogeneously in the aluminum matrix. Due to not applied plastic deformation under this condition, the aluminum matrix presents scarce dislocations and defects that contribute to the precipitation of clusters [18]. However, after 300 min of aging, precipitates with needle-shaped morphology and length between 10 and 30 nm are observed (Fig. 3b). In addition, high

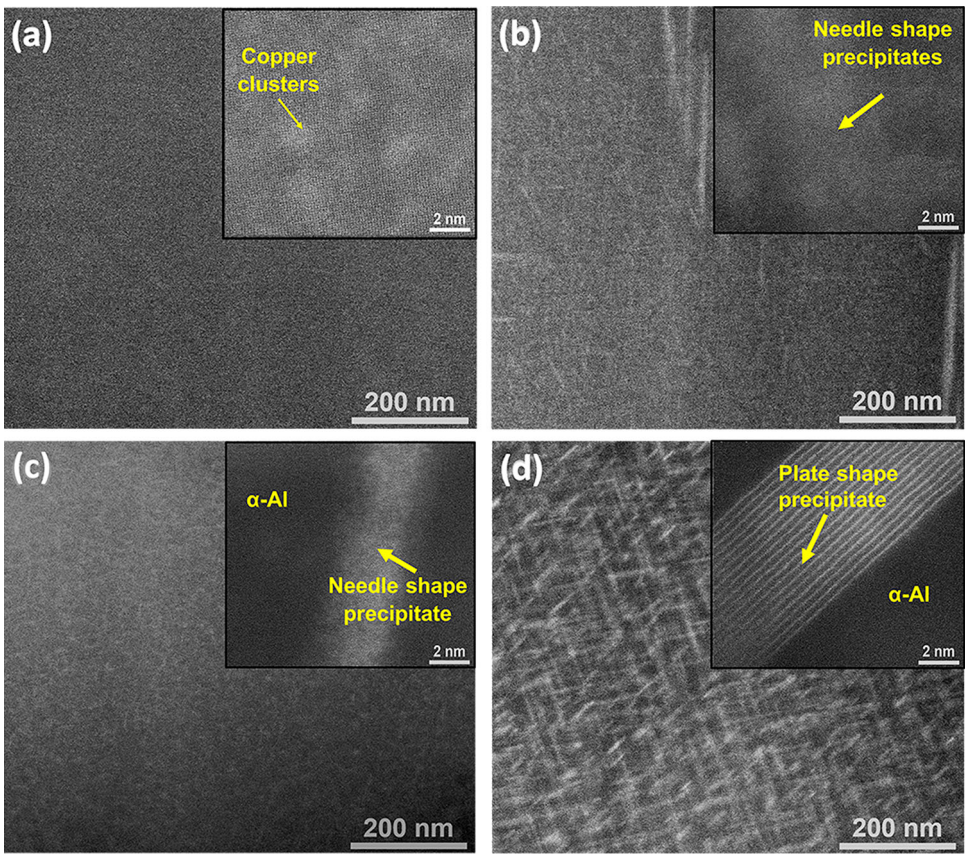

Figure 3 HAADF-STEM images of alloys aged at 195°C during different times. Non-deformed: 30 min **a**; 300 min **b**. Deformed by cold-rolling to 30%: 30 min **c**; 600 min **d**.

magnifications on the same sample also showed precipitates with a length between 0.5 and 2 nm.

Comparing the HAADF-STEM images of the deformed 2024 aluminum alloy and aged for 30 min (Fig. 3c) with the non-deformed alloy (Fig. 3a), the results suggest that plastic deformation promotes the formation of precipitates with needle-shaped morphology, between 20 and 40 nm in length, from the beginning of the precipitation. However, after aging for 600 min (Fig. 3d), the presence of plate-like shape precipitates with a length between 60 and 140 nm and 30 and 80 nm were observed. Therefore, for the deformed and non-deformed alloys, differences in morphology and size of the precipitates are observed, which suggests a different precipitation sequence.

Figure 4 shows TEM images of deformed and non-deformed aged alloys in bright field mode (BF) with their corresponding selected area electron diffraction (SAED) patterns obtained by nano-beam diffraction (NBD). The image of the non-deformed alloy aged for 30 min (Fig. 4a) consists of Cu-rich zones (dark zones) homogeneously distributed into the aluminum matrix. The SAED pattern shows bright spots corresponding to the aluminum matrix and diffuse streaking attributed to the precipitates. The simulation performed indicated that bright spots match in the $[001]_{\alpha\text{-Al}}$ (Fig. 4b). The low-intensity spots and faint streaks correspond to $[001]_{GPB\text{-II}}$, $[010]_{GPB\text{-II}}$, and $[010]_{S'}$.

The simulation determined that GPB-II exhibits an orthorhombic structure, a space group Cmmm with lattice parameters a = 12.12, b = 4.04, and c = 4.04 Å [19]. Additionally, the S′ phase herein identified corresponds to the one reported by Perlitz–Western: orthorhombic structure (Cmcm space group) and lattice parameters a = 4.0, b = 9.23, and c = 7.14 Å [20, 21]. The weak intensity detected of $\{110\}_{GPB\text{-II}}$ reflections suggests that they arise because of the Mg and Cu atoms ordering into the FCC aluminum matrix. The weak intensity of the S′ precipitate (Al_2CuMg) spots indicates that this precipitate has a low numeric density [20, 22].

When the aging time increases from 30 to 300 min, the volume fraction of the S′ phase in the aluminum matrix increases, as can be deduced from the diffraction pattern of non-deformed alloy (Fig. 4c, d). The half crosses located around the forbidden $\{110\}_{Al}$ reflections are characteristic of this type of precipitate [3]. In addition, stronger streaking connecting habit planes (200)(020), (−220)(2–20), (−200)(0–20), and streaks at 1/3 and 2/3 $\{220\}_{Al}$ parallel to [100] matrix direction were observed. GPB-II spots were not observed; instead, streaks corresponding to S′ phase were identified [23]. The high intensity of the streaks suggests an increment in the precipitate size consistent with the HAADF/BF-STEM images, as shown previously in Fig. 3.

To better understand the effect of plastic deformation on the precipitation sequence, SAED patterns of the deformed alloy are shown. After aging for 30 min, the SAED pattern results indicate that different phases coexist with the aluminum matrix (Fig. 4(e–f)). These phases are GPB-II (with the same features previously mentioned) and θ′′-Al_3Cu phase with tetragonal structure, P4/mbm spatial group, and lattice parameters of a = b = 4.06 and c = 7.80 Å, located in 1/3 and 2/3 $\{200\}_{Al}$ [24]. In addition, the reflections located between 1/2 $\{220\}_{Al}$ and $\{200\}_{Al}$ planes are attributed to θ′ (Al_2Cu) with tetragonal structure, I-4m2 spatial group with lattice parameters of a = b = 4.04 and c = 5.8 Å [20]. However, when aging for 600 min, the diffraction pattern of deformed alloy only showed reflections corresponding to the S′ phase (Fig. 4g, h).

It is worth noting that the Al-Cu alloy formed G.P zones, θ′′ and θ′ phases [18]. However, in addition to Cu/Mg ratio, in the Al-Cu-Mg system alloy, the deformation energy and dislocations produced by plastic deformation generate competitive precipitations between G.P zones, θ′′, θ′, GPB-II zones and S′ phase, respectively [17]. As seen in the diffraction pattern of the cold-rolled alloy (Fig. 4f), θ′′ and θ′ phases precipitated after aging to 30 min. The fact that these phases were identified in the diffraction pattern suggests that the formation of G.P zones could occur within a few minutes. Thus, under experimental conditions performed in this work, the results indicate that when the 2024 aluminum alloy is deformed plastically, θ′′ and θ′ precipitate sooner than the S′ phase. In addition, GPB-II zones promote the precipitation of the metastable S′ phase, which subsequently generates stable precipitation at 600 min aging (Fig. 4h).

Instead, when plastic deformation by cold-rolling is not applied, competition between precipitations does not occur, and only the S′ precipitation mechanism prevails. In this case, GPB-II zones precipitate on the aluminum matrix at 30 min aging, coexisting with S′ phase (Fig. 4a, b). However, its precipitation

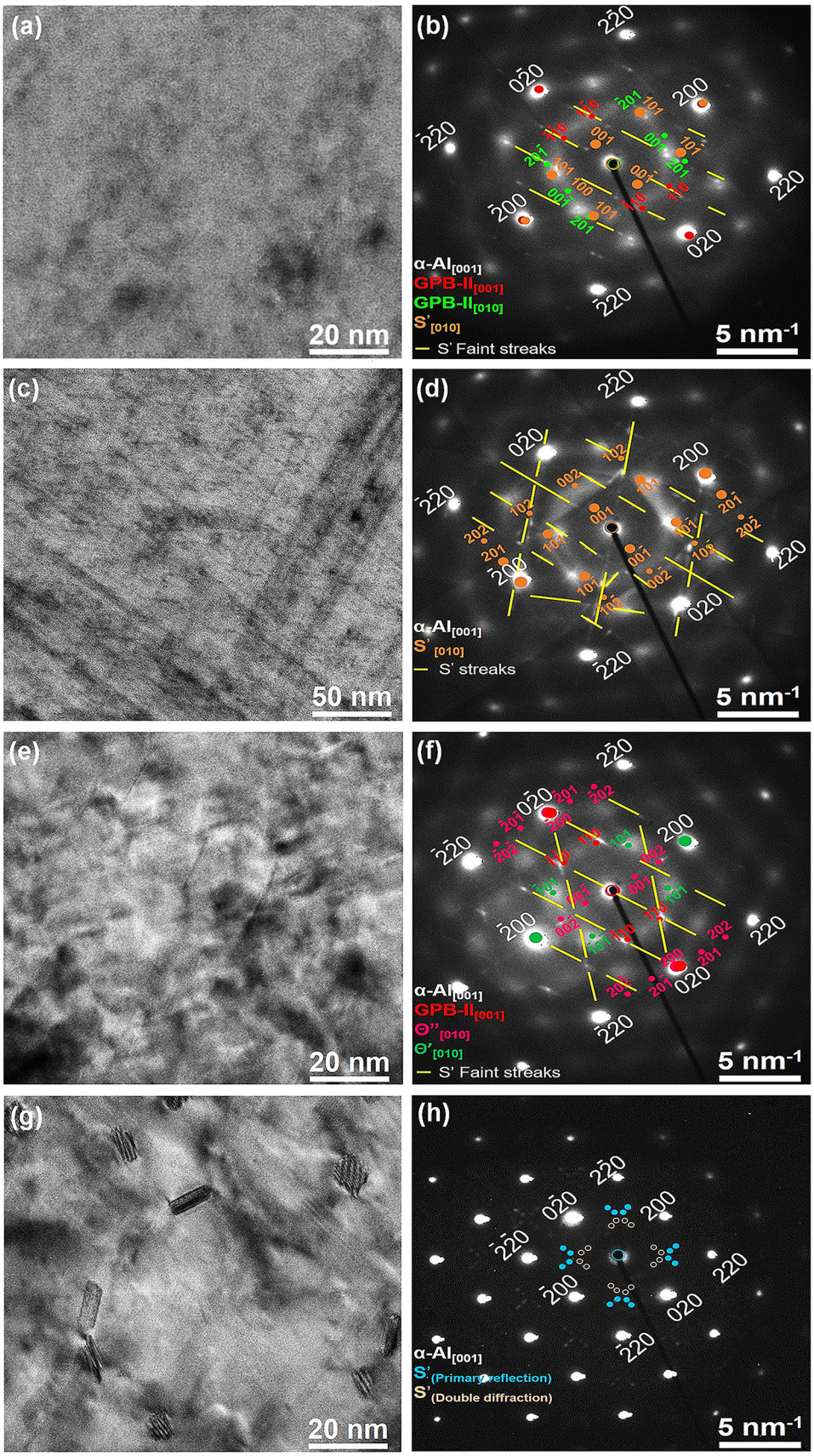

Figure 4 TEM-BF images and their corresponding SAED patterns with structural simulations of phases for 2024 alloy, aged during different times at 195°C. Non-deformed alloy: 30 min **a**–**b**; 300 min **c**–**d**. Deformed by cold-rolling to 30%: 30 min **e**–**f**; 600 min g–**h**.

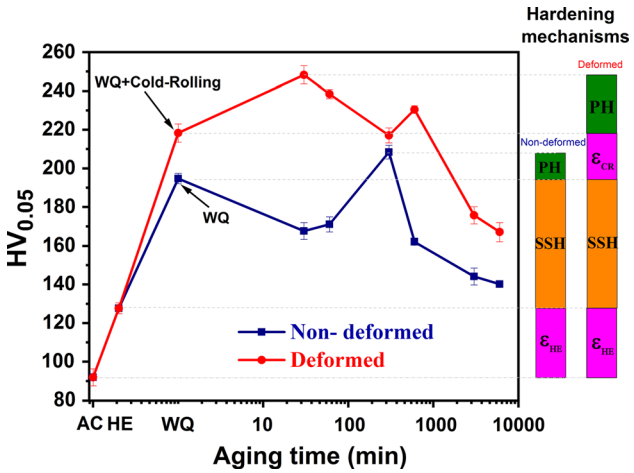

Figure 5 Microhardness curves and hardening mechanisms present during processing. The symbology represents the following: AC: as-cast, HE: hot extruded, WQ: water quenched, ε_{HE}: strain hardening by extrusion, SSH: solid solution hardening, ε_{CR}: strain hardening by cold-rolling, PH: precipitation hardening.

finishes to a shorter aging time (300 min) to comparison with plastically deformed alloy.

Correlation between processing, microstructure, and precipitation sequence on the microhardness

Vickers microhardness values (HV) were studied for the different processing conditions and aging heat treatment in deformed and non-deformed alloys. The results have been correlated with the microstructure and precipitation sequence obtained. In this regard, Fig. 5 shows the evolution of the Vickers microhardness and the hardening mechanisms for each processing step. As can be seen, the behavior of the microhardness is related to the processing condition and the precipitated phases that occur during aging.

The alloy exhibited the lowest HV value (92 ± 4) in the as-cast condition because the aluminum matrix consists of α-Al dendrites. However, the generation of dislocations, fragmentation, and dispersion of the interdendritic phases by the hot-extrusion process increases the hardness to 128 ± 3HV. In the non-deformed alloy, after the SHT, the alloy reached a microhardness of 195 ± 3 HV. This behavior was attributed to the solid-solution hardening effect caused by the presence of Cu and Mg atoms inside the metallic matrix. After the SHT and cold-rolling, the alloy reached 218 ± 5 HV; this hardness increment is attributed to solid-solution and strain hardening combined. Besides, precipitation hardening occurs in both alloys at different aging times. Thus, plastic deformation shifts the maximum hardening peak to shorter aging times and higher microhardness. The HV curve for the deformed alloy exhibited double-peak age-hardening: the first one occurred at 30 min (248 HV ± 5), and is attributed to the coexistence of GPB-II zones, θ'' and θ' phases. The second one occurred after aging for 600 min (230 HV ± 2) due to S' phase precipitation.

It is worth mentioning that a drop in the microhardness was observed between 30 and 300 min aging between both hardening peaks. This phenomenon is attributed to a transition stage due to the formation of S' phase metastable variants. After the second hardening peak, the HV value considerably decreases until the end of the aging time.

In contrast, the non-deformed alloy observed a drop of microhardness between 0 and 30 min aging. This behavior occurs because of the dissolution of CuMg clusters and further formation of GPB-II zones that act as nucleation sites to the S' phase formation, which is responsible for the maximum hardening peak detected at 300 min (208 HV ± 4). After achieving the maximum hardness, a decrement in the microhardness behavior occurs. The above results suggest that the plastic deformation delays the overaging stage; for non-deformed alloy, this begins after 300 min, while in the deformed alloy it occurs after 600 min.

In addition, the mechanical properties are usually affected by dislocations density and the type and size of precipitates [25, 26]. Thus, the microhardness results suggest that plastic deformation notably influences this behavior due to the formation of dislocations, which generates a high energy state in the alloy that promotes preferential precipitation. Compared to other studies [9, 11], this research shows higher HV values at a shorter aging time. Therefore, depending on the conditions used, different types and sizes of precipitates form during the aging of the alloy, which indicates that the processing conditions carried out in this work substantially improve the precipitation hardening.

Discussion

Precipitation sequence for non-deformed and deformed alloy

Regarding the quenching temperature, preliminary results of the current work showed that in non-deformed 2024 alloy, the microhardness value of alloy quenched in water at 60 °C is higher (195 HV ± 3) than alloy quenched in water at 20 °C (165 HV ± 3). The above evidence could indicate that quenching temperature contributes significantly to forming the first hardening peak with higher HV values and a shorter aging time due to changes in the precipitation sequence. In this sense, a study performed in an Al-4.5%Cu alloy shows similar results, quenching in water at 40°C shows that the first hardening peak occurs to shorter aging time (45 min) compared with quenching water at 25°C; where the hardening peak was obtained to longer aging time (80 min) [27]. However, we must do a deeper investigation on the effect of quenching on different temperatures.

On the other hand, it is worth noting that the increase in the HV is mainly attributed to the rapid formation of CuMg clusters promoted by the presence of supersaturated vacancies upon quenching [26–28]. Moreover, as mentioned earlier, the drop in HV values during aging is related to the dissolution of the CuMg clusters [29]. Studies by DSC have demonstrated that CuMg cluster dissolution occurs between 160–250 °C [30, 31]. Therefore, the dissolution phenomenon is responsible for HV values decrement at the beginning of the AHT in the non-deformed alloy (30 min aging). In this sense, TEM analyses in the non-deformed alloy indicated that GPB zones coexist with S′ phase after aging for 30 min. Taking into account this observation, the time–temperature transformation diagram for the Al-Cu-Mg alloy system indicates the formation of CuMg clusters + GPB2/S“ and GPB2/S” + S after 30 and 60 min, respectively [20, 32, 33].

However, the NBD pattern (Fig. 4b) for the GPB zones reported in this work is consistent with the structure established by Kovarik (named GPB-II), and it can be ideally considered like mono/double layers of Cu atoms [19]. Thus, considering the HV value obtained at 30 min aging (168 HV ± 4), GPB-II zones could have a limited contribution to the alloy hardening. Furthermore, after 30 min aging, GPB-II zones were not identified; diffraction spots of GPB-II zones showed in Fig. 4b suggest that such zones may act as nucleation sites for the S′ phase. After aging for 300 min, S′/S phases were detected (Fig. 4d), which is consistent with the maximum hardening peak observed in the HV curve of Fig. 5. Furthermore, the maximum hardening peak occurs faster than the second hardening peak of the deformed alloy. This phenomenon could be influenced by the velocity of solute diffusion and dislocations available to facilitate the precipitation. It is worth noting that the non-deformed alloy exhibits minimum internal stresses and fewer dislocations than the deformed alloy. The minimum distortion of crystal lattice facilitates the diffusion of the Mg atoms and could be a dominant factor for the S′ precipitation. Hence, the continued drop of the HV values observed in Fig. 5 after 600 min might be explained by the coherency loss of S′ precipitates due to overaging. Thus, the following precipitation sequence for non-deformed samples is proposed: αSSS → CuMg clusters → GPB-II zones/S′/ → S.

In contrast, as was shown in Fig. 5, the evolution of the HV curve with the aging time for deformed samples differs from the non-deformed samples. This difference suggests that the applied deformation shifted the maximum hardening peak to a shorter aging time. Besides, a second hardening peak also was observed. The above results reveal that plastic deformation affects both the precipitation sequence and the HV values reached. Before AHT, the deformed samples without aging (t = 0 min) presented a higher HV value than non-deformed samples. This value is attributed to the strain hardening, which increases the dislocations density. During the aging of the deformed alloy, the microhardness is increased considerably.

Similarly, Deschamps et al. [34] showed that in Al-2.5Cu-1.5 Mg (wt. %) alloy, extremely stable CuMg clusters are formed within a few minutes during the aging. However, after 20–30 min, the first S precipitates or closely related phases are detected. These precipitates become the dominant hardening phase at 540 min in the aged peak. Compared with our research, the formation time of S precipitates is similar to the measured for deformed samples in the present work (600 min aging). However, the evolution of the microhardness curve is different due to the relation between Cu/Mg and the deformation applied. Thus, as was shown in Table 1, the content of Cu and Mg is 4.789 and 1.432 wt. %, respectively.

Under this condition, the phase diagram indicates that the possible phases obtained are α-Al, θ′ and S′ [20]. However, the results suggest that in addition to the above, CuMg clusters, GPB-II, and θ′′ were also obtained, indicating that cold-rolling significantly influences the phases formed. In this sense, it is known that in aluminum alloys, the degree of applied deformation makes every possible precipitated phase compete for the preferential nucleation sites and solute atoms [11, 35]. Hence the precipitation reaction is dominated by the phase that can minimize interphase boundary energy and form defects that reduce the nucleation energy barrier [6].

The above may explain the formation of the first hardening peak observed in the microhardness curve of deformed alloy, which demonstrates an accelerated precipitation reaction, possibly due to θ″ formation. Because of this, it has been reported that external stress applied to Al-5Cu alloy accelerates precipitation of θ″ [36]. Therefore, according to Fig. 4f, the θ″ precipitation in Al-Cu-Mg alloy is not exclusive of Al-Cu alloys. The degree of deformation and the Cu/Mg ratio is responsible for forming these precipitates in Al-Cu-Mg alloy. Besides, the θ′ phase coexists in the aluminum matrix, which arises from θ″ (Al_3Cu) transformation due to the segregation of Cu elements, which further enriches the Al atom and neighboring Cu-rich layers. The Cu-rich interlayer distance is reduced from three to two atom layers [37].

It is worth highlighting that the coexistence of θ″ and θ′ phases have been reported in an aluminum alloy without Mg content [38]. However, although the activation energy for Mg diffusion in aluminum is lower than the Cu diffusion [32], the high density of dislocations can act as atomic diffusion paths in the deformed alloy, which accelerates the aging process by promoting the formation of GPB zones or phase transformations of θ′ and S′ [39]. The above behavior could also be related to the lower Cu atomic size facilitating its segregation in a distorted aluminum lattice, favoring the formation of the θ′ phase. Since θ′ exhibits higher stability (− 3.9934 eV/atom) than S′ phase (− 3.4615 eV/atom), it is more feasible its precipitation at a short aging time [40]; therefore, the θ′ phase could nucleates heterogeneously on dislocations thus lowering the strain energy [41]. Furthermore, it has been reported that the high density of dislocations produced by deformation is detrimental to the S′ phase's thermal stability [42]. This phenomenon could also contribute to θ″ phase formation and subsequent precipitation of θ′.

The drop in the microhardness of the deformed alloy after aging for 30 min could be considered a transition stage that contributes to the formation of the S′ phase. This transformation could occur when the GPB-II zones are previously formed; for instance, these zones could act as nucleation sites for the S′ phase formation [19]. Additionally, the release of strain from the aluminum matrix and the decrease in dislocations density upon aging favor the S′ phase [43]. Moreover, isothermal aging experiments have shown that Mg promotes the S′ precipitation [44], i.e., Mg diffuses towards the θ′ precipitates, favoring the S′ phase formation. In this sense, the formation enthalpy of S′ (-0.2501 eV/atom) is lower than θ′ (-0.2033 eV/atom), which indicates that S′ has a stronger alloying ability relative to θ′, being S′ favored by low dislocations density [40]. Therefore, the S phase could be the origin of the second hardening peak at 600 min aging and the delay of the overaging due to the S′ phase precipitation. After 600 min decreases the HV value because of the precipitates coarsening and its coherency loss with aluminum matrix. Thus, the results obtained suggest that the precipitation sequence proposed for the deformed alloy is the following: α_{SSS} → CuMg clusters → GPB-II/ θ′′ → θ′ → S′ → S. This sequence indicates that the deformation by cold-rolling 30% is responsible for the formation of transition phases such as GPB-II zones, θ″ and θ′ before achieving the total precipitation of S phase.

Relationship between the plastic deformation and microhardness

For non-deformed alloy, the precipitation mechanism is simple. However, the microhardness values are lower than deformed alloy, and a high density of dislocations was not generated. There is no competition by nucleation sites between phases to carry out the precipitation, which was corroborated in Fig. 5 by the drop of microhardness immediately after starting the aging. This phenomenon was also found during the aging of the 2024-T3 alloy without applying external stress. The drop microhardness was attributed to dissolution GPB zones that occur until the first 10 min of aging [17]. In contrast with this work, evidence of GPB zones after starting the aging was not found in alloy without cold-rolling, so that the

results obtained were attributed to dissolution of CuMg clusters [9].

Nevertheless, similar to our results, it is related to dissolution when the aging time is increased. Under the experimental condition performed in this work, the above event originates decreasing microhardness from 195 until 168 HV during the first 30 min aging (Fig. 5). This behavior provides evidence of the importance of dislocations in the precipitation mechanism. Due to in non-deformed alloy by cold-rolling less density of dislocations is available, the competition between phases formation is inhibited because less distortion in the crystal lattice is carried out. Therefore, less distortion in the metallic matrix favors the dissolution of CuMg clusters previously formed after the quenching. Another important event is related to the formation of GPB-II zones, which begin to precipitate after 30 min aging, which occurs because of the processing conditions used: hot extrusion, solubilization, and quenching at 60°C. This processing sequence generates the following in the alloy: (1) small distortion in the crystal lattice with low-density dislocations, (2) strain release and homogenization of solute atoms inside the aluminum matrix, (3) generation of vacancies and formation of CuMg clusters. Thus, the CuMg clusters get dissolved during aging while the solute atoms get reordered inside the metallic matrix, thus forming GPB-II zones. Later, the GPB-II could act as nucleation zones for S′ precipitation, increasing the microhardness from 168 to 208 HV at 300 min aging.

For the deformed alloy, the results obtained showed a relationship between the precipitation mechanism and mechanical properties. The plastic deformation could change the precipitation mechanism during aging, which affects the microhardness of the 2024 aluminum alloy. This result agrees with another study of Al–Cu–Mg alloy where the precipitation mechanisms are influenced by external stress during the creep-aging, which enhances the precipitation process, resulting in the change of physical properties of the studied alloy [45]. In addition, it has been established that work hardening increases the strength (yield and ultimate tensile strength increase), which is accompanied by a decrease in ductility [46]. Significant similarities of the above results are related to the external stress applied. In our work, this external stress is applied through the cold-rolling process, which generates dislocations that strengthen the alloy. In the case of cold-rolling alloy, the formation mechanism for GPB-II could be the same as that in alloy without cold-rolling. However, due to the higher dislocations density and distortion of metallic lattice, remnant solute atoms diffuse and precipitate on dislocation lines from where the formation of the θ″ and θ′ phases is initiated. In this sense, taking into account the microhardness results and hardening stages presented in Fig. 5. It was shown that the microhardness behavior is complex in the deformed alloy, and the values more elevated, especially during the first 30 min aging is increased from 195 to 248 HV due to fine precipitates as θ′′ and θ′, mainly. Although GPB-II also is present during the first stage of aging, this phase possibly was not precipitated by the effect of plastic deformation but contributed to the mechanism precipitation to carry out the formation of some variants S′, which generates a drop in the microhardness from 248 to 212 HV, being later increased this value until 230 HV due to precipitation of S′. It is worth noting that in this work, S′ variants are metastable phases that decrease the microhardness after 30 min aging. Such variants correspond to the 2, 3, and 4 type variants according to simulated diffraction patterns reported by Wang and Starink [20].

Conclusions

The plastic deformation to 30% modifies the precipitation sequence and the evolution of the microhardness with the aging time of the 2024 aluminum alloy. This behavior contributes to achieving higher hardness in a shorter aging time. Thus, the plastic deformation favors the following precipitation sequence α_{SSS} → CuMg clusters → GPB-II/θ′′/θ′/ → S′ → S. This mechanism accelerates the precipitation after 30 min aging due to the formation of GPB-II zones, θ″ and θ′ phase and delays the overaging caused by S′ phase precipitation up to 600 min aging. However, when plastic deformation was not applied, the precipitation sequence was α_{SSS} → CuMg clusters → GPB-II/S′/ → S. This mechanism suggests that dissolution of CuMg clusters until 30 min occurs and GPB-II zones were formed during the aging process. Subsequently, hardening of the alloy is attained by precipitation of the S′ phase when aged for 300 min.

Acknowledgments

Project Supported by the Sectorial Research Fund for Education, CONACYT, A1-S-32226. J.C. Guia-Tello expresses his gratitude to the National Council of Science and Technology in Mexico (CONACYT) for the postdoctoral scholarship provided. The authors are deeply grateful to Karla Campos Venegas for her valuable support with SEM/EDAX analysis, Ernesto Guerrero Lasterjette for his assistance in the DRX studies, Oscar Solis Canto for his support in the sample preparation by FIB, and Carlos Elias Ornelas Gutierrez for his technical assistance in analyzing samples by STEM and TEM, respectively.

Author contributions

GT contributed to methodology, investigation, and writing-original draft. GR contributed to formal analysis and supervision. RC contributed to analysis and DRX data interpretation. MP contributed to MEB Analysis. RER contributed to TEM Study. GH contributed to STEM Study. MD and EG contributed to microhardness test and data analysis. GS and GA contributed to english revision and critical comments of the manuscript. MS contributed to project leader and approval of the final submitted version of the manuscript.

Declarations

Conflict of interest The authors declared that they have no conflict of interest.

References

[1] Parel TS, Wang SC, Starink MJ (2010) Hardening of an Al–Cu–Mg alloy containing types I and II S phase precipitates. Mater Des 31:S2–S5. https://doi.org/10.1016/j.matdes.2009.12.048

[2] Wang SQ, Schneider M, Ye HQ, Gottstein G (2004) First-principles study of the formation of Guinier-Preston zones in Al–Cu alloys. Scripta Mater 51:665–669. https://doi.org/10.1016/j.scriptamat.2004.06.018

[3] Li S, Zhang J, Yang J, Deng Y, Zhang X (2014) Influence of Mg contents on aging precipitation behavior of Al–3.5Cu–xMg alloy. Acta Metall Sin 27(1):107–114. https://doi.org/10.1007/s40195-014-0033-7

[4] Liu Y, Teng F, Cao FH, Yin ZX, Jiang Y, Wang SB, Shen PK (2019) Defective GP-zones and their evolution in an Al-Cu-Mg alloy during high-temperature aging. J Alloys Compd 774:988–996. https://doi.org/10.1016/j.jallcom.2018.10.061

[5] Winkelman GB, Raviprasad K, Muddle BC (2007) Orientation relationships and lattice matching for the S phase in Al–Cu–Mg alloys. Acta Mater 55:3213–3228. https://doi.org/10.1016/j.actamat.2007.01.011

[6] Ünlu N, Gable BM, Shiflet GJ, Starke EA Jr (2003) The effect of cold work on the precipitation of Ω and θ′ in a ternary Al-Cu-Mg alloy. Metall Mater Trans A 34:2757–2769. https://doi.org/10.1007/s11661-003-0177-y

[7] Quan LW, Zhao G, Gao S, Muddle BC (2011) Effect of pre-stretching on microstructure of aged 2524 aluminium alloy. Trans Nonferrous Met Soc China 21:1957–1962. https://doi.org/10.1016/S1003-6326(11)60956-4

[8] Rodgers BI, Prangnell PB (2016) Quantification of the influence of increased pre-stretching on microstructure-strength relationships in the Al-Cu-Li alloy AA2195. Acta Mater 108:55–67. https://doi.org/10.1016/j.actamat.2016.02.017

[9] Ferragut R, Somoza A, Positron, (1999) Age–hardening and precipitation in predeformed 2024 (Al–Cu–Mg) alloy. Phys Stat Sol A 175:R1–R2. https://doi.org/10.1002/(SICI)1521-396X(199909)175:13.0.CO;2-3

[10] Singh S, Goel DB (2005) Influence of thermomechanical aging on fatigue behaviour of 2014 Al-alloy. Bull Mater Sci 28:91–96. https://doi.org/10.1007/bf02704225

[11] Zhao YL, Yang ZQ, Zhang Z, Su GY, Ma XL (2013) Double-peak age strengthening of cold-worked 2024 aluminum alloy. Acta Mater 61:1624–1638. https://doi.org/10.1016/j.actamat.2012.11.039

[12] Zuiko I, Kaibyshev R (2018) Aging behavior of an Al-Cu-Mg alloy. J Alloys Compd 759:108–119. https://doi.org/10.1016/j.jallcom.2018.05.053

[13] Li HZ, Liu RM, Liang XP, Deng M, Liao HJ, Huang L (2016) Effect of pre-deformation on microstructures and mechanical properties of high purity Al-Cu-Mg alloy. Trans Nonferrous Met Soc China 26:1482–1490. https://doi.org/10.1016/S1003-6326(16)64253-X

[14] Sadeghi-Nezhad D, Mousavi Anijdan SH, Lee H, Park N, Nayyeri MJ, Jafarian HR, Shin W (2020) The effect of cold rolling, double aging and overaging processes on the tensile property and precipitation of AA2024 alloy. J Mater Res Technol 9(6):15475–15485. https://doi.org/10.1016/j.jmrt.2020.11.005

[15] Huda Z, Taib NI, Zaharinie T (2009) Characterization of 2024–T3: An aerospace aluminum alloy. Mater Chem Phys 113:515–517. https://doi.org/10.1016/j.matchemphys.2008.09.050

[16] DeRose JA, Balkowiec A, Michalski J, Kurzydlowski KJ, Schmutz P, Suter T (2012) Aluminium alloy corrosion of aircraft structures, modelling and simulation. In: DeRose JA, Sute T, Hack T, Adey R (eds) Microscopic and macroscopic characterisation of an aerospace aluminium alloy (AA2024). WIT press, USA, pp 23–38

[17] Lin YC, Xia YC, Jiang YQ, Zhou HM, Li LT (2013) Precipitation hardening of 2024–T3 aluminum alloy during creep aging. Mater Sci Eng A 565:420–429. https://doi.org/10.1016/j.msea.2012.12.058

[18] Zhu XH, Lin YC, Wu Q, Jiang YQ (2020) Effects of aging on precipitation behavior and mechanical properties of a tensile deformed Al-Cu alloy. J Alloys Compd 843:155975. https://doi.org/10.1016/j.jallcom.2020.155975

[19] Kovarik L, Gouma PI, Kisielowski C, Court SA, Mills MJ (2004) A HRTEM study of metastable phase formation in Al–Mg–Cu alloys during artificial aging. Acta Mater 52:2509–2520. https://doi.org/10.1016/j.actamat.2004.01.041

[20] Wang SC, Starink MJ (2005) Precipitates and intermetallic phases in precipitation hardening Al–Cu–Mg–(Li) based alloys. Int Mater Rev 50:193–215. https://doi.org/10.1179/174328005X14357

[21] Petschke D, Lotter F, Staab TEM (2019) Revisiting the crystal structure of the equilibrium S (Al_2CuMg) phase in Al–Cu–Mg alloys using X-ray absorption spectroscopy (XAFS). Materialia 6:100341. https://doi.org/10.1016/j.mtla.2019.100341

[22] Gupta AK, Gaunt P, Chaturvedi MC (1987) The crystallography and morphology of the S'-phase precipitate in an Al(CuMg) alloy. Philos Mag A 55(3):375–387. https://doi.org/10.1080/01418618708209875

[23] Abis S, Massazza M, Mengucci P, Riontino G (2001) Early ageing mechanisms in a high-copper AlCuMg alloy. Scripta Mater 45:685–691. https://doi.org/10.1016/s1359-6462(01)01080-6

[24] Wiengmoon A, Pearce JTH, Chairuangsri T, Isoda S, Kurata H, Saito H (2013) HRTEM and HAADF-STEM of precipitates at peak ageing of cast A319 aluminium alloy. Micron 45:32–36. https://doi.org/10.1016/j.micron.2012.10.009

[25] Lin YC, Dong WY, Zhu XH, Wu Q, He YJ (2020) Deformation behavior and precipitation features in a stretched Al–Cu alloy at intermediate temperatures. Mater 13:2495. https://doi.org/10.3390/ma13112495

[26] Iloabachie ICC (2018) Effect of water quenching temperatures on the hardness of Al-4.5%Cu. Research & Reviews: J Eng Technol 7(3):122–130

[27] Wang SC, Starink MJ (2004) The assessment of GPB2/S″ structures in Al–Cu–Mg alloys. Mater Sci Eng A 386:156–163. https://doi.org/10.1016/s0921-5093(04)00913-x

[28] Kovacks I, El Sayed H (1976) Point defects in metals. J Mater Sci 11:529–559. https://doi.org/10.1007/bf00540934

[29] Tolley A, Ferragut R, Somoza A (2009) Microstructural characterisation of a commercial Al–Cu–Mg alloy combining transmission electron microscopy and positron annihilation spectroscopy. Philos Mag 89(13):1095–1110. https://doi.org/10.1080/14786430902889674

[30] Wang SC, Starink MJ, Gao N (2006) Precipitation hardening in Al–Cu–Mg alloys revisited. Scripta Mater 54:287–291. https://doi.org/10.1016/j.scriptamat.2005.09.010

[31] Starink MJ, Gao N, Davin L, Yan J, Cerezo A (2005) Room temperature precipitation in quenched Al–Cu–Mg alloys: a model for the reaction kinetics and yield strength development. Philos Mag 85(13):1395–1417. https://doi.org/10.1080/14786430412331333374

[32] Gao N, Davin L, Wang SC, Cerezo A, Starink MJ (2002) Precipitation in stretched Al-Cu-Mg alloys with reduced alloying content studied by DSC, TEM and Atom Probe. Mater Sci Forum 396–402:923–928

[33] Starink MJ, Gao N, Yan J (2004) The origins of room temperature hardening of Al–Cu–Mg alloys. Mater Sci Eng A 387–389:222–226. https://doi.org/10.1016/j.msea.2004.01.085

[34] Deschamps A, Bastow TJ, de Geuser F, Hill AJ, Hutchinson CR (2011) In situ evaluation of the microstructure evolution during rapid hardening of an Al–2.5Cu–1.5Mg (wt.%) alloy. Acta Mater 59:2918–2927. https://doi.org/10.1016/j.actamat.2011.01.027

[35] Hornobogen E (2000) Formation of nm-size dispersoids from supersaturated solid solutions of aluminium. Mater Sci Forum 331–337:879–888

[36] Fu S, Yi DQ, Liu HQ, Jiang Y, Wang B, Hu Z (2014) Effects of external stress aging on morphology and precipitation behavior of θ″ phase in Al-Cu alloy. Trans Nonferrous Met Soc China. https://doi.org/10.1016/S1003-6326(14)63345-8

[37] Zhang P, Wang Y (2017) A study on the nucleation mechanism of nano-scale precipitates of 7055 aluminum alloy. NANO Brief Rep Rev. https://doi.org/10.1142/S1793292017501478

[38] Elgallad EM, Zhang Z, Chen XG (2017) Effect of quenching rate on precipitation kinetics in AA2219 DC cast alloy. Phys B: Condens Matter 514:70–77. https://doi.org/10.1016/j.physb.2017.03.039

[39] Ning AL, Liu ZY, Zeng SM (2006) effect of large cold deformation on characteristics of age-strengthening of 2024 aluminum alloys. Trans Nonferrous Met Soc China. https://doi.org/10.1016/S1003-6326(06)60388-9

[40] Zhang J, Huang YN, Mao C, Peng P (2012) Structural, elastic and electronic properties of θ (Al_2Cu) and S (Al_2-CuMg) strengthening precipitates in Al–Cu–Mg series alloys: First-principles calculations. Solid State Commun 152:2100–2104. https://doi.org/10.1016/j.ssc.2012.09.003

[41] Sehitoglu H, Foglesong T, Maier HJ (2005) Precipitate effects on the mechanical behavior of aluminum copper alloys: part I Experiments. Metall Mater Trans A 36:749–761. https://doi.org/10.1007/s11661-005-1006-2

[42] Wang X, Liu Z, Bai S, Lin L, Ye C, Wang H (2016) Enhanced heat resistance of Al-Cu-Mg alloy by a combination of pre-stretching and underaging. J Mater Eng Perform 25(9):3793–3801. https://doi.org/10.1007/s11665-016-2152-y

[43] Shih HC, Ho NJ, Huang JC (1996) Precipitation behaviors in Al-Cu-Mg and 2024 aluminum alloys. Metall Mater Trans A 27:2479–2494. https://doi.org/10.1007/bf02652342

[44] Ringer SP, Hono K (2000) Microstructural evolution and age hardening in aluminium alloys: atom probe field-ion microscopy and transmission electron microscopy studies. Mater Charact 44:101–131. https://doi.org/10.1016/S1044-5803(99)00051-0

[45] Lin YC, Liu G, Chen MS, Li J, Zhou M, Zhou HM (2015) Effects of two-stage creep-aging processing on mechanical properties of an Al–Cu–Mg alloy. Mater Des 79:127–135. https://doi.org/10.1016/j.matdes.2015.04.047

[46] Lin YC, Jiang YQ, Xia YC, Zhang XC, Zhou HM, Deng J (2014) Effects of creep-aging processing on the corrosion resistance and mechanical properties of an Al–Cu–Mg alloy. Mater Sci Eng A 605:192–202. https://doi.org/10.1016/j.msea.2014